

CFD evaluation of hydrophobic feedstock bench-scale fermenters for efficient high agitation volumetric mass transfer

Richard Marx, Huolong Liu, Seongkyu Yoon* and Dongming Xie*

Department of Chemical Engineering, University of Massachusetts Lowell, Lowell, MA 01854

Key Words: CFD, PBM, stirred-tank bioreactor, hydrophobic feedstock, multiphase flow

* Corresponding authors:

Seongkyu Yoon, Department of Chemical Engineering, University of Massachusetts Lowell, 1 University Ave. Lowell MA 01854 Email: Seongkyu_Yoon@uml.edu

Dongming Xie, Department of Chemical Engineering, University of Massachusetts Lowell, 1 University Ave. Lowell MA 01854 Email: Dongming_Xie@uml.edu

Abbreviations:

BC Boundary condition

$k_L a$ Volumetric mass transfer coefficient

MUSIG Multiple size group

PBM Population balance modeling

TSF Timescale factor

vvm Volume of gas per volume of unaerated liquid per minute

Abstract

A new biomanufacturing platform combining intracellular metabolic engineering of the oleaginous yeast *Yarrowia lipolytica* and extracellular bioreaction engineering provides efficient bioconversion of plant oils/animal fats into high-value products. However, predicting the hydrodynamics and mass transfer parameters is difficult due to the high agitation and sparging required to create dispersed oil droplets in an aqueous medium for efficient yeast fermentation. In the current study, commercial computational fluid dynamic (CFD) solver Ansys CFX coupled with the MUSIG model first predicts two-phase system (oil/water and air/water) mixing dynamics and their particle size distributions. Then, a three-phase model (oil, air, and water) utilizing dispersed air bubbles and a polydispersed oil phase was implemented to explore fermenter mixing, gas dispersion efficiency, and volumetric mass transfer coefficient estimations ($k_L a$). The study analyzed the effect of the impeller type, agitation speed, and power input on the tank's flow field and revealed that upward-pumping pitched blade impellers (PBI) in the top two positions (compared to Rushton-type) provided advantageous oil phase homogeneity and similar estimated $k_L a$ values with reduced power. These results show good agreement with the experimental mixing and $k_L a$ data.

1. Introduction

Yarrowia lipolytica, when combined with intracellular metabolic engineering and extracellular bioreaction engineering, can synthesize a wide range of valuable metabolites with U.S. FDA GRAS (“generally recognized as safe”) status [1]. This makes *Y. lipolytica* an ideal choice for efficient bioconversion of oils/fats into high-value pharmaceuticals and food additives such as citric acid and wax esters [2-5]. This strictly aerobic yeast requires efficient oxygen transfer for cell growth and lipid production [6], and oil substrates must be well-dispersed in the aqueous medium with high agitation for small oil droplets to attach to the surface of *Y. lipolytica* cells for bioconversion. Cellular and bioreaction engineering determines the overall production rate, necessitating understanding the oil particles’ size, morphology, and bioreactor position (relative to the yeast). The oil’s lower density, hydrophobic nature, and water insolubility necessitate strong agitation, as mixing can be the fermentation’s limiting factor. This high agitation requires baffles to reduce tangential flow, whose flow impedance exacerbates the high power consumption [7]; balancing these demands makes CFD study a useful tool for designing an efficient and productive fermenter configuration.

Fermentation mixing efficiency is vital for lipid biodegradation performance [8]. Triple-impeller aerobic fermenters have demonstrated energy-efficient gas-liquid mass transfer but have liquid mixing disadvantages [9, 10]. Modeling the oil and air interfacial areas for mass transfer and mixing helps design these processes better [11]. Population balance modeling (PBM) has helped overcome experimental bubble size deviation [12-14] and has dramatically progressed to help predict particle sizes for high-shear and complex flow patterns of dispersed liquid-liquid systems [12, 15, 16]. Recently, PBMs were applied to three phases to understand particle size implications [17]. This is similar to the three phases in our fermenter, where sparging impacts the immiscible feedstock mixing.

CFD modeling has widely studied fermenters, and the high power-to-volume ratios (P/V) needed to overcome incomplete mixing or mass transfer have been well demonstrated [9, 18-20]. Despite common CFD studies of fermenter gas-liquid mass transfer or liquid-liquid mixing, a gap exists in considering both simultaneously.

Despite disadvantages, Rushton-type impellers are still commonly used [14]. Pitched blade impellers were implemented in the top and middle positions to improve liquid mixing and gas holdup, targeting improved product fermentation efficiency (Liu et al., 2021). This study presents our recent modeling effort to demonstrate the inherent obstacles of sufficient hydrophobic feedstock mixing with adequate mass transfer for three impeller setups. The three-phase simulations completed with ANSYS CFX 2020 R2, which are representative of the experimental hydrodynamic parameters, are compared with key mass transfer and mixing measurements. The study found, and correlated to noteworthy experimental data, that upward-pumping pitched blade impellers in the top and middle position and a Rushton impeller on the bottom operated at 1200 RPM increased mixing and mass transfer parameters previously correlated with improved valuable metabolite synthesis [5].

2. Materials and Methods

2.1. Fermenter setup

CFD simulations were based on previous *Y. lipolytica* fed-batch fermentations with vegetable oil in the medium in a 1-L working volume glass bioreactor (Sartorius Stedim UniVessel®) with key geometrical details displayed in Figures 1B and 1C [5]. UniVessel® 2-L impellers (3 x 53 mm OD evenly-spaced (24 mm center-to-center)) discs were preferentially used to improve mixing. Gas holdup and bubble diameter values were determined empirically with 1 L of tap water. For oil mixing experiments, 5% (by volume) of the water was replaced with corn oil, and images were captured with a Canon EOS 6D Mark II. Experimental volumetric mass transfer coefficient values ($k_L a_e$) were based on the oxygen uptake rate (OUR) during *Y. lipolytica* fermentations controlled at a constant dissolved oxygen level (C_o). This results in equal OUR and oxygen transfer rate (OTR) when C_o is controlled at a constant value:

$$OUR = OTR = k_L a_e (C_o^* - C_o) \quad (1)$$

where C_o^* and C_o represent the saturated (no cellular uptake) and actual dissolved oxygen concentration (with cellular oxygen uptake). The OUR was determined by an oxygen mass balance of the bioreactor while accounting for the working reactor volume:

$$OUR = \frac{\dot{m}_{in}(O_2) - \dot{m}_{out}(O_2)}{V} \quad (2)$$

1 Allowing the experimental $k_L a$ to be estimated by:

$$k_L a_e = \frac{OUR}{(C_o^* - C_o)} \quad (3)$$

2 2.2. CFD geometry and mesh generation

3 Fluid domain booleans were created with multiple frames of reference (MFR) domains
4 around each impeller and set with the same angular velocity. This method implicitly
5 matches the outer, stationary domain solutions along a single boundary surface without
6 external iterations [21]. The geometry was then symmetrically halved to reduce the size
7 and meshed with a linear element order 1.25e-3 m tetrahedral element mesh with inflation
8 layers added to the stationary and rotating domains near the rotating surfaces and
9 discharge regions [22]. The mesh was then adapted to the sliding mesh (SM) approach
10 to examine if it would better capture fermenter flow dynamics.

11 2.3. Simulation and Experimental Design

12 CFD simulations were conducted with different impeller setups and speeds to elucidate
13 which operational conditions may provide improved fermentation. First, simplified two-
14 phase, oil-water (OW) simulations were completed to understand and quantify mixing by
15 population balance modeling of the oil phase with a free-slip wall boundary condition (BC)
16 imposed on the liquid surface. Next, two-phase, air-water (AW) simulations were
17 performed utilizing population balance equation-multiple size group (MUSIG) modeling to
18 describe the air bubbling through the water with a degassing BC imposed on the liquid
19 surface [23]. This approach allowed an average air bubble size to be calculated and
20 implemented as a fixed-diameter air particle in the three-phase simulations. The three-
21 phase simulations were run with the addition of a headspace and normal-speed air outlet
22 (Figure 1A). In these three-phase simulations, water remains the continuous phase, oil is
23 a polydispersed (MUSIG) phase, and air is a fixed-diameter dispersed phase. For all
24 simulations, uniform yeast particle distributions are assumed due to their small size and
25 similar density to water, allowing the suspension to be modeled with flow characteristics
26 of the continuous phase [24].

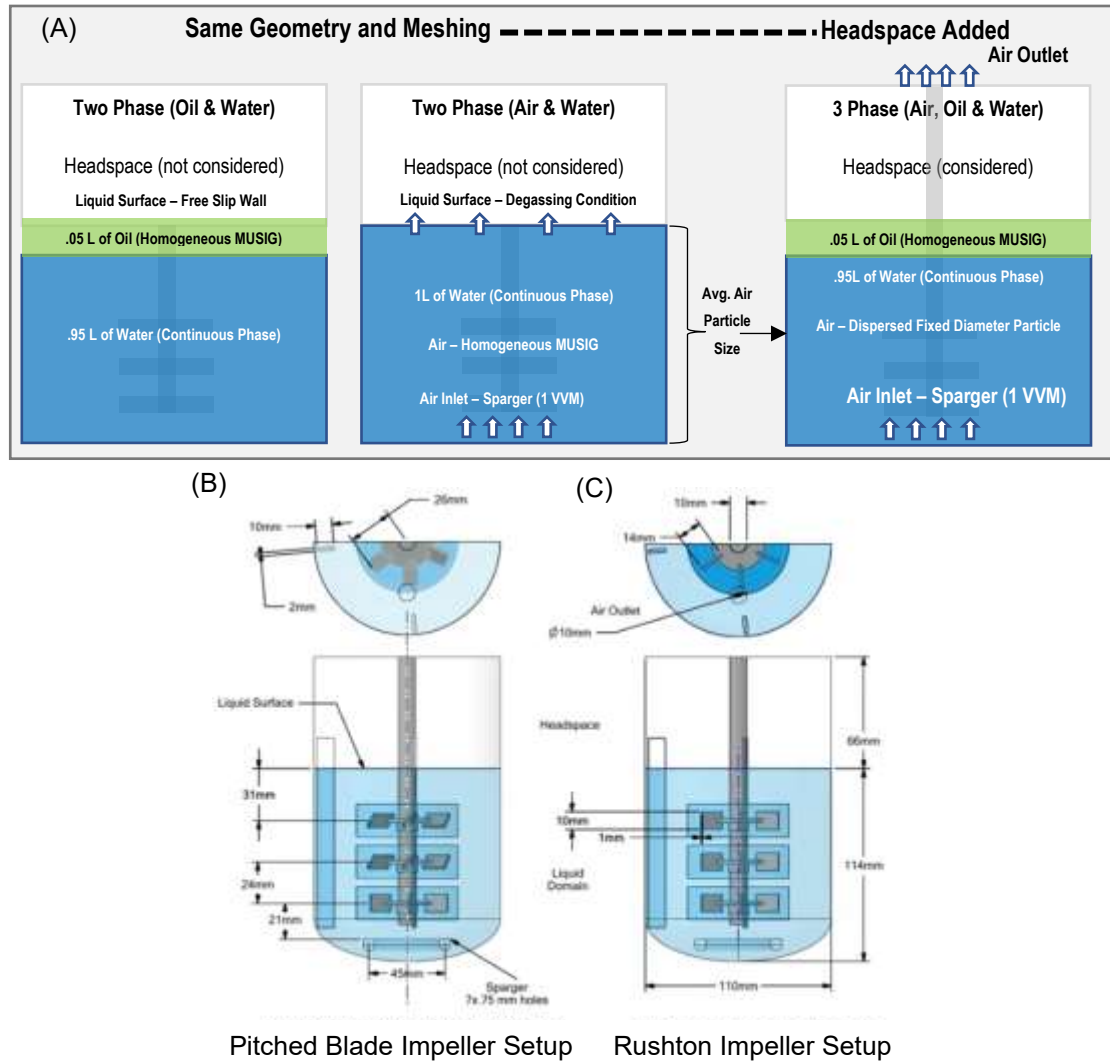


FIGURE 1

2.4. Simulation setup

Water and oil were specified for the oil/water simulations with 0.95 and 0.05 volume fractions to study mixing. The water volume fraction was 1 for the air and water simulations. For three-phase simulations, the fluid domain was extended to a 224-mm height to include the headspace, and the volume fractions were adjusted accordingly to model 1L of liquid (95% water and 5% oil by volume). The tank's walls, impellers, and baffles had no-slip conditions and utilized volume fractions to select scalable wall functions for the continuous phase for near-wall treatment. The continuous phase used k-epsilon while disperse-phased phases utilized the Dispersed Phase Zero Equation turbulence models with turbulent dispersion forces accounted for by Favre Averaged Drag

Force (Dispersion Coefficient = 1). A normal speed inlet BC was specified on the ring sparger holes with an expression-calculated velocity from the specific aeration rate vvm (the ratio of air volumetric flow rate (L min^{-1}) to the bioreactor liquid volume (L)). A similar expression was utilized to mass balance the air outlet velocity with zero specified for the oil and water velocities. A conservative timescale factor (TSF) of 1 was used for all simulations except where explicitly noted. Reduced TSFs (.25 and .50) were also tested to reduce experimental deviation for high RPM simulations. For dynamic simulations, a fixed .001 s physical timescale run for 120 s or until the oil reached $\pm 5\%$ of the steady-state concentrations.

2.5. Numerical solution

Convergence criteria of a 1×10^{-5} root mean square (RMS) residual target was used; however, with the high turbulence in these systems, a few “hot spots” may stall residuals for valid solutions. If the RMS residual target was not met, the simulations were run on the Massachusetts Green High-Performance Computing Center with a 14-day run time for solutions (generally resulting in >130,000 iterations). The local parallel calculations on the LINUX cluster were performed on 64 nodes on a 512 GB Red Hat 8 core. This run time ensured that volume fractions and $k_L a$ values were not changing outside the quasi-steady-state solution range with additional timesteps. Multiple criteria focusing on the stabilization of critical parameters (i.e., gas holdup- or $k_L a$) accompanied by reduction of residuals and energy dissipation have been previously utilized for multi-impeller systems [25-27].

2.6. Modeled equations to predict fermenter hydrodynamics and performance

Table 1 shows the CFD-modeled equations with a complete background in the supplemental information.

2.7. CFD estimation of volumetric mass transfer coefficients

In combination with CFD results, Higbie's penetration theory described the gas/liquid mass transfer. This model assumes mass transfer occurs during many short and repeated gas bubble collisions, with the continuous phase generating turbulence as it continuously renews [27]. The mass transfer resistance (k_L) was estimated by

$$k_L = \frac{2\sqrt{D}}{\sqrt{\pi}} \left(\frac{\rho_L * \varepsilon_c}{\mu_l} \right)^{\frac{1}{4}} \quad (4)$$

1 where μ_l is the viscosity of water, and D is the diffusion coefficient of oxygen. The
2 interfacial surface area of the dispersed gas phase (a_g) is calculated by

$$a_g = 6 \frac{\alpha_g}{d_{bg}} \quad (5)$$

3 where α_g is the gas volume fraction and d_{bg} is the average air bubble size. Equations 29
4 and 30 were applied to an air isovolume between 0–1 volume fractions. Successful $k_L a$
5 estimations have been demonstrated for fermentation processes under relatively low
6 agitation speeds [14, 20, 26-28]; however, this paper aims to provide strongly aerobic
7 fermentation mass transfer behavior analysis with high agitation speeds, *i.e.*, up to 1200
8 RPM stirring speeds in a 1-L three-impeller vessel. The resulting variables were combined
9 with a constant (C_k) to calibrate mass transfer coefficients:

$$k_L a_{PT} = C_k k_L a_g \quad (6)$$

10 C_k values were determined by:

$$C_k = \frac{k_L a_e}{k_L a_g} \quad (7)$$

11 which compares experimental yeast fermentation oxygen mass transfer ($k_L a_e$) to CFD-
12 derived estimates with the same bioreactor geometry and operating conditions. Typically,
13 a 1-L working volume *Y. lipolytica* fermentation with three Rushton (3R) impeller setup at
14 1200-RPM stirring speed at 30 °C, 1.0 vvm aeration, and a dissolved oxygen of 20%
15 air saturation ($C_o = 0.2C_o^*$) has an observed OUR $\approx 120 \text{ mmol L}^{-1} \text{ h}^{-1}$. Since the C_o^* in
16 water at 30°C is 7.54 mg L^{-1} or 0.24 mmol L^{-1} , based on Equation (3), the estimated
17 $k_L a_e$ for these conditions is 636 hr^{-1} . Therefore C_k helps to calibrate $k_L a_{PT}$ to the actual
18 bioreactor performance.

3. Results and Discussion

3.1. Two-phase (oil and water) mixing analysis

Previously [5], two-impeller mixing analyses showed large oil particles gathering in the reactor's top center and adjacent to impeller discharges. Two three-impeller configurations (Figure 1B and 1C) were implemented to improve mixing and analyzed with water and 5% (v/v) corn oil CFD simulations for 200, 500, 1000, and 1200-RPM stirring speeds. Typical for Ruston impellers, buoyant oil particles accumulated near the shaft above the top impeller (Figure 2A) [29] at low stirrer speeds, and the higher stirrer speeds' impeller tip power caused more significant shear resulting in smaller oil droplets and better distribution [30]. The 3R simulations demonstrate that increasing stirring speed helps distribute the oil partially down the bioreactor; however, the oil tends to get "stuck" in the middle of the reactor with high-concentration pockets off the impeller discharges, limiting oil accessibility.

The top impeller's size, position, relative height to the liquid surface, and flow pattern are controlling parameters for pulling down buoyant particles [31]. By substituting two upward pumping impellers, the floating oil particles are swept to the outside and eventually drawn down (Figure 2F–H) [32]. With 1000- or 1200-RPM stirring speeds, the mixing significantly improved due to stronger circulation loops developing down the reactor sides, resulting in a more homogeneous oil distribution reflected in the oil uniformity numbers. Typical for liquid-liquid dispersions in water, the average Sauter mean diameter of the oil droplets decreased with increasing system homogeneity [12]. The smaller particles and improved mixing of the oil and water with the PBI setup at 1200-RPM stirring speed have been correlated to improved *Y. lipolytica* fermentation for bioconversion of TAG oil into specific high-value products and closely match the improved experimental production [5]. However, two-phase oil and water simulations make simplifications, mostly the omittance of air, the impact of which will be reviewed in section 3.3.

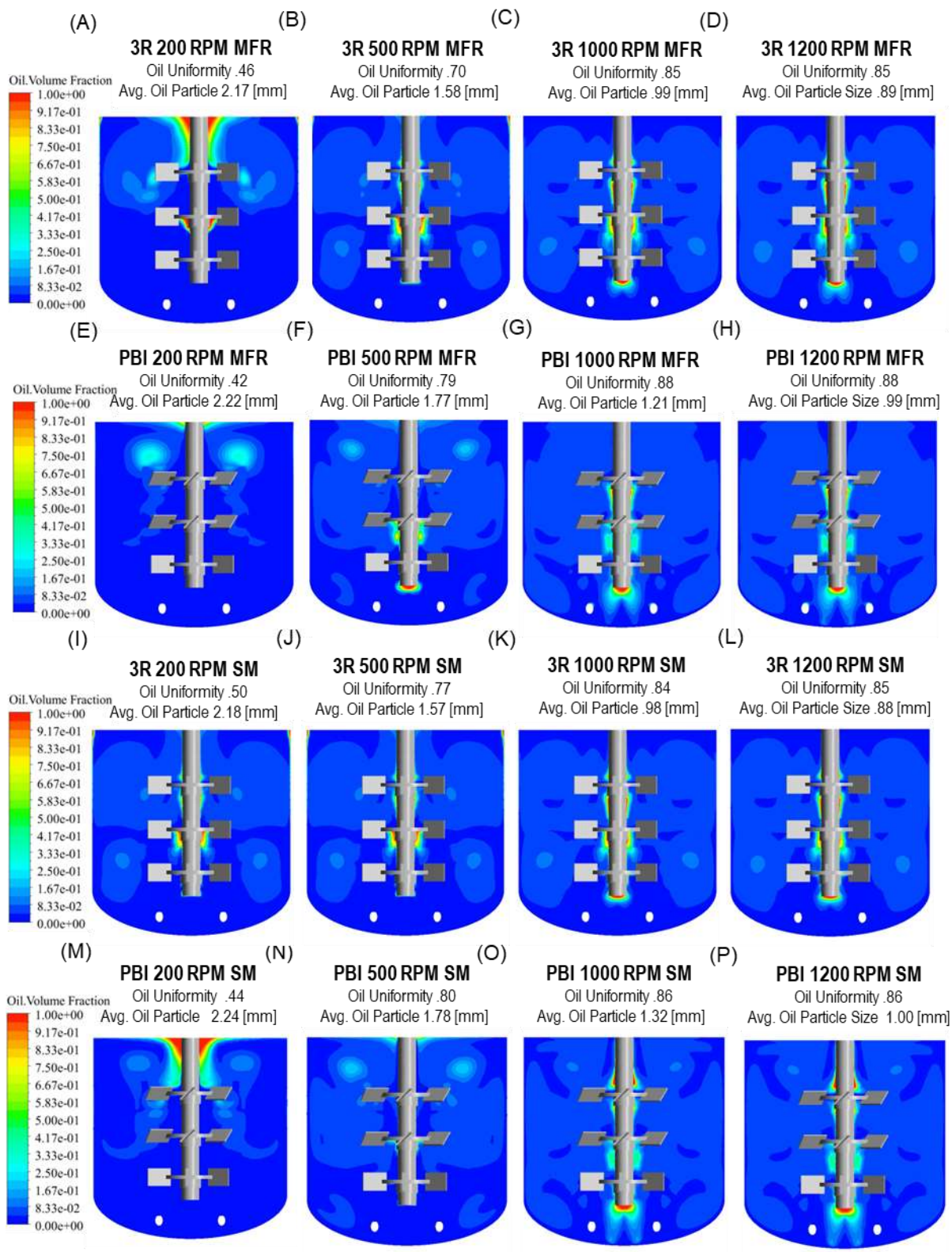


FIGURE 2

1 1-L bioreactor mixing experiments with water and 5% (v:v) corn oil were conducted to
 2 validate the oil-water mixing simulations, and the results are shown in Figure 3. CFD
 3 mixing times were also compared, with the 3R setup having slightly longer mixing times
 4 at equivalent power inputs than the PBI setup. Experimentally, the bench-scale mixing
 5 times are almost instantaneous, and a large scale would better highlight these trends.

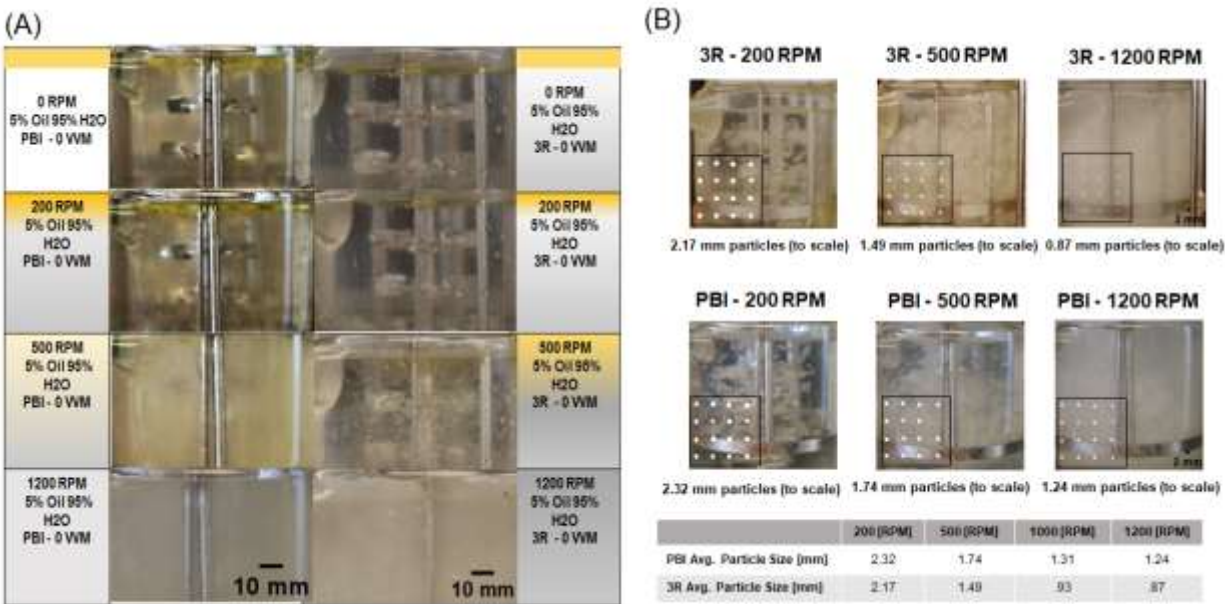


FIGURE 3

A Figure 2 and 3A comparison demonstrates that ~1000 RPM is needed to utilize the reactor volume fully, and although CFD often underestimates stirred tank mixing due to turbulence model inadequacies [23], a clear stirrer speed indication is provided. The MFR (Figure 2A–H) and SM approach (Figure 2I–P) produced similar mixing results, indicating improved mixing and homogeneity with the PBI setup. The oil phase utilized the Luo and Svendsen break-up model, which model extensions [33] have highly enhanced turbulent vegetable oil-in-water emulsion CFD predictions [34]. In addition, the widely used Schiller and Naumann drag correlation only considers spherical particles and cannot correctly represent interface deformability force changes [35]. For oil and water interactions, lift was considered negligible due to the similar density and small oil droplet sizes [12], but lift models such as the model by Frank et al. [36] should be reviewed for their larger oil droplet implications. An alternative approach to better correlate CFD with experimental results would be to tune F_B [25] encouraging easier oil break-up and diffusion. However,

for longer fermentation runs, the oil particles adhere to the shaft, baffles, and impellers (like the CFD models), indicating that the process is in multiple ways well-characterized by the steady-state, oil-water CFD modeling.

3.2. Two-phase (air and water) particle size characterization

CFD modeling next examined the vessel's gas holdup and air particle size distributions with the MFR and SM approach utilizing air and water with a degassing BC. The average air bubble size is a crucial derived parameter to help provide a similar gas interfacial area to an air PBM while using a computationally less-intensive dispersed phase for the three-phase models. The CFD models indicate that the average air bubble size decreases as power input increases due to increased shear and turbulence. Average air bubble sizes displayed in Figure 3B were completed without oil, which clouds the reactor, hindering photographic bubble size verification. Experimental high-speed camera images were compared to the average bubble sizes to ensure reasonable agreement. High-speed camera images for 200-, 500- and 1200-RPM stirring speeds are displayed in Figure 3B (1000-RPM stirring speeds omitted due to 1200-RPM similarity) and compared to the average particle size (to-scale) for reference (Figure 3B).

Figure 4A compares CFD vs. Xie et al. correlation-derived gas holdup values, which generally show good agreement except for the 3R 1000 and 1200 RPM results [37]. The holdup discrepancies can not be solely attributed to some known lab-scale MFR inaccuracies for high impeller-to-tank diameter ratios [38], as the SM approach also displays significant experimental holdup deviation, which might be expected without turbulent dispersion force and drag coefficient modifications [39]. There appear to be two contributing factors: Power input impacts the simulation's accuracy as simulations with P/Vs less than $6,000 \text{ W m}^{-3}$ provide reasonable holdup results. Secondly, the degassing BC may ignore close-to-surface, top-impeller, high-velocity, impeller-shaft vortexes that trap air in the reactor [38]. The degassing BC acts as a water-free-slip wall and air outlet, disallowing headspace air reentry. Instead, a pressure distribution based on flow surface height variations is used, with a fixed reference pressure point automatically set for the domain. Ignoring these vortexes and the inability for surface air drawdown appears to contribute to the degassing BC showing reduced CFD holdup for these high-agitation

1 Rushton simulations. Reducing the TSF for MFR models only modestly (~10%) reduced
2 the CFD-experimental discrepancy. This lower Rushton holdup could indicate potential
3 impeller flooding evinced by poorly dispersed gas that rises directly along the shaft, or
4 high impeller speeds may cause vortices behind the impeller blades, dispersing the air
5 [43] but require a more detailed study of the phenomenon.

6 Experimentally, the 3R and PBI setups produce similar low stirring speed gas holdup,
7 with the PBI setup showing better energy efficiency for similar holdup values above 5,000
8 W m^{-3} (Figure 4B). This more efficient holdup may indicate that the PBI setup reaches
9 effective gas dispersion limited by the bubble break-up/coalescence equilibrium with less
10 power than the 3R [10]. These findings are consistent with multiple studies noting higher
11 gas holdup utilizing upward-pumping in the top two positions and a radially dispersing
12 impeller on the bottom but are limited to lower P/V ratios ($P/V < 4000 \text{ W m}^{-3}$) [37, 40, 41]
13 with similar two-impeller trends [42]. With the noted degassing BC limitations, simulations
14 considering the headspace were completed (MFR and SM approach) and showed
15 significant improvement for the high-power ($>6,000 \text{ W m}^{-3}$) Rushton simulations. All
16 three-phase simulations utilize the headspace to ensure holdup accuracy and a realistic
17 boundary condition for the oil. The degassing BC should not be applied for liquid
18 dispersed phases as they only see the BC as an exit, which can create an erroneous
19 mass imbalance. To further reduce the CFD and experimental gap, a 0.5 TSF was utilized
20 for the high-power headspace simulations and showed slightly overestimated but
21 reasonable gas holdup values compared to the experimental results (similar to the three-
22 phase results in Figure 4C). Looking at relevant power inputs required for adequate
23 hydrophobic feedstock fermentation mixing ($>6000 \text{ W/m}^3$), the 1200-RPM PBI setup
24 showed increased gas holdup around the shaft and top two impellers with flow
25 recirculation loops down the sides. This upper impeller's superior gas utilization efficiency
26 is due to small air bubbles recirculating without moving through the impeller disc region
27 [43]. This advantageous air recirculation flow pattern should help improve three-phase oil

- 1 mixing and provide energy efficiency by producing similar gas holdup values with less
- 2 power input (P/V), an essential scale-up factor.

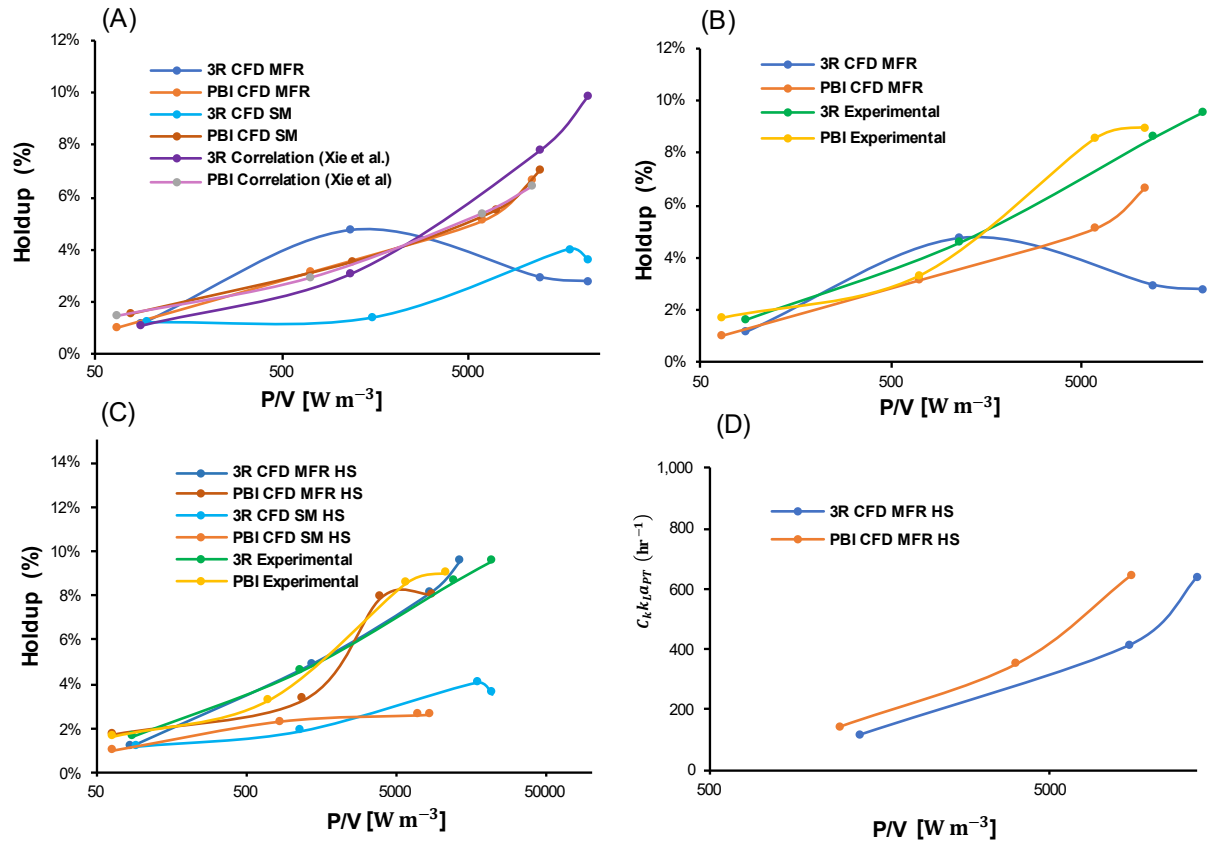


FIGURE 4

3.3. Three-phase (air, oil and water) volumetric mass transfer

The simplified two-phase simulations, either air-water or oil-water, point to liquid-liquid mixing advantages and more efficient gas distribution with the PBI setup. Three-phase (air, oil, and water) simulations with the headspace were then completed with a reduced 0.5 TSF for the higher 1000- and 1200-RPM stirring speeds for both the MFR and SM approaches. The SM approach showed poor CFD-experimental correlation, indicating future work should tune parameters impacting air coalescence in these high-power input fermenter conditions. The MFR method showed better experimental correlation and will be the only method discussed further. With three phases, the PBI setup showed improved mixing with 10% higher oil uniformity, as seen visually in Figure 5D. The added sparging-induced turbulence helps further distribute the oil away from the shaft and impellers. Liquid-liquid mixing remains challenging to quantify, but the PBI setup at a 1200-RPM

1 stirring speed pulls ~84% of the oil down into the original liquid domain (compared to only
2 63% for the 3R impeller setup at 1200-RPM stirring speeds), which we interpret as a
3 general indicator of good fermentation mixing. The 3R impeller setup has large amounts
4 of oil driven to the bottom and into the headspace region, which may reduce the
5 accessibility of the yeast cells to the oil substrate and lead to decreased productivity in
6 the oil fermentation [5]. Three-phase simulation gas holdup follows the same flow patterns
7 as the two-phase simulations, as air and water are the dominant physics mechanisms.
8 Including the headspace generally increased the holdup values and showed improved
9 experimental correlation for the 1000 and 1200 RPM simulations (Figure 4C). Although
10 the Rushton simulations feature slightly higher holdup values, the air is primarily grouped
11 around the shaft and under the impellers, which limits access. The PBI setup generally
12 shows more air circulating outside this impeller diameter area, which we believe benefits
13 the fermentations (Figure 5H).

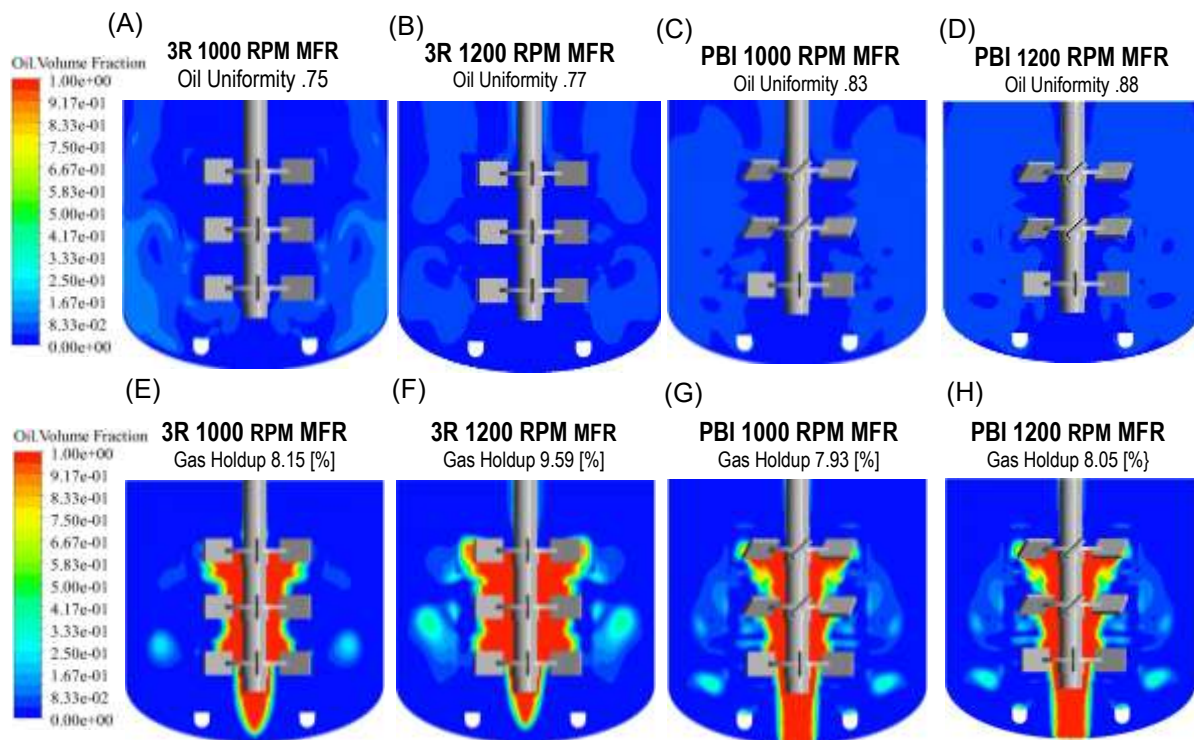


FIGURE 5

14 Figure 4B displays the CFD estimated $k_L a$ values for the MFR three-phase simulations,
15 which show good agreement with experimental results. 500–750 h^{-1} $k_L a$ values are well
16 established for this type of bench-scale process at 1200-RPM stirring speeds similar to

1 industry-scale mass transfer characteristics, typically corresponding to 100–150 mmol
2 $\text{L}^{-1} \text{h}^{-1}$ oxygen transfer rates. In addition, the 500-RPM stirring speed simulations show
3 a reasonable $k_L a$ range (117–143 h^{-1}) for this type of process [45-47]. Slight increases
4 compared to previous studies were expected due to the use of 2L-sized impellers in the
5 1L reactor, which leads to higher P/V values. In addition, PBI setups have previously
6 demonstrated higher $k_L a$ values with reduced power [48] with good mass transfer and
7 flow field scalability from the laboratory to pilot-scale when compared to 3R impeller
8 setups [49]. These trends correlate with improved *Y. lipolytica* fermentation with oil
9 substrate under these conditions [5]. Overestimation of $k_L a$ by the single bubble size was
10 demonstrated previously [26] and is accounted for with C_k . The single bubble size used
11 for the air phase does not account for bubble-bubble interactions and bubble turbulence
12 as captured by the population balance equations, impacting multiple parameters.
13 Viscosity also affects mass transfer and may need to be considered separately [21] as it
14 impacts droplet/bubble size in population balances [50], which would impact mass
15 transfer.

16 Having demonstrated the PBI setup's mixing and energy efficiency benefits, it was
17 desired to understand how lower (.5 and .75 vvm) and higher (1.5 and 2.0 vvm) aeration
18 rates impacted the 1200 RPM PBI setup CFD model. The lower aeration rates reduced
19 holdup by up to 37% (with a similar $k_L a$ reduction) while maintaining similar mixing
20 characteristics and oil distribution. The high vvm simulations produced up to a 25%
21 increase in holdup (with a similar $k_L a$ increase), which seemed promising initially, but a
22 more detailed analysis revealed that ~90% of the additional air was bunched around the
23 shaft and impellers. As previously discussed with the 3R setup, this bunching negatively
24 impacts the oil mixing, seen in an oil uniformity reduction (~10%). Given the lack of
25 additional, accessible air and reduced oil mixing, these aeration modifications don't look
26 to provide measurable production benefits but need to be experimentally verified.

4. Concluding Remarks

A three-phase CFD model has been used to study a highly agitated fermenter's mass transfer and mixing characteristics utilizing hydrophobic feedstock such as plant oils. The three-phase (air, oil, and water) model was able to use both air bubble size and solution data to improve convergence and provide highly agreeable $k_L a$ values with experimental and literature data. The pitched-blade impeller setup at higher stirring speeds improved mixing characteristics with similar mass transfer while using reduced power compared to Rushton impeller setups. This reduced-power setup could have significant monetary implications at the industrial scale and certainly deserves further investigation.

Acknowledgments

This project is supported by the National Science Foundation (#1911480). The authors thank Dr. Iman Mirzaee for providing CFD simulation feedback and suggestions. In addition, we would like to thank Mr. Jiansong Qin and Ms. Elif Kurt for helping run the 1-L bioreactor experiments.

Conflict-of-Interest Statement

The authors declare no commercial or financial conflicts of interest.

Data Availability Statement

The data that support the findings of this study are available from the corresponding author upon reasonable request.

5. References

- [1] Zieniuk, B., Fabiszewska, A., *Yarrowia lipolytica*: a beneficial yeast in biotechnology as a rare opportunistic fungal pathogen: a minireview. *World J Microbiol Biotechnol* 2018, 35, 10.
- [2] Xie, D., Jackson, E., Zhu, Q., Sustainable source of omega-3 eicosapentaenoic acid from metabolically engineered *Yarrowia lipolytica*: from fundamental research to commercial production. *Applied Microbiology & Biotechnology* 2015, 99, 1599-1610.
- [3] Liu, N., Liu, B., Wang, G., Soong, Y.-H. V., *et al.*, Lycopene production from glucose, fatty acid and waste cooking oil by metabolically engineered *Escherichia coli*. *Biochemical Engineering Journal* 2020, 155.
- [4] Soong, Y.-H. V., Zhao, L., Liu, N., Yu, P., *et al.*, Microbial synthesis of wax esters. *Metabolic Engineering* 2021, 67, 428.
- [5] Liu, N., Soong, Y.-H. V., Mirzaee, I., Olsen, A., *et al.*, Biomanufacturing of value-added products from oils or fats: A case study on cellular and fermentation engineering of *Yarrowia lipolytica*. *Biotechnology and Bioengineering* 2021, 118, 1677.
- [6] Xie, D., Integrating Cellular and Bioprocess Engineering in the Non-Conventional Yeast *Yarrowia lipolytica* for Biodiesel Production: A Review. *Frontiers in Bioengineering and Biotechnology* 2017.
- [7] Kamla, Y., Bouzit, M., Hadjeb, A., Arab, I. M., Beloudane, M., CFD study of the effect of baffles on the energy consumption and the flow structure in a vessel stirred by a Rushton turbine. *Mechanika* 2016, 22, 190.
- [8] Matran, R. M., Galaction, A.-I., Blaga, A. C., Turnea, M., Cașcaval, D., Distribution of Mixing Efficiency in a Split-Cylinder Gas-Lift Bioreactor with Immobilized *Yarrowia Lipolytica* Cells Used for Olive Oil Mill Wastewater Treatment. *Chemical Engineering Communications* 2016, 203, 666-675.
- [9] Puthli, M. S., Rathod, V. K., Pandit, A. B., Gas-liquid mass transfer studies with triple impeller system on a laboratory scale bioreactor. *Biochemical Engineering Journal* 2005, 23, 25-30.
- [10] Gogate, P. R., Beenackers, A. A. C. M., Pandit, A. B., Multiple-impeller systems with a special emphasis on bioreactors: a critical review. *Biochemical Engineering Journal* 2000, 6, 109-144.
- [11] Luo, H., Svendsen, H. F., Theoretical model for drop and bubble break-up in turbulent dispersions. *AIChE Journal* 1996, 42, 1225-1233.
- [12] Naeeni, S. K., Pakzad, L., Droplet size distribution and mixing hydrodynamics in a liquid-liquid stirred tank by CFD modeling. *International Journal of Multiphase Flow* 2019, 120.
- [13] Laakkonen, M., Alopaeus, V., Aittamaa, J., Validation of bubble breakage, coalescence and mass transfer models for gas-liquid dispersion in agitated vessel. *Chemical Engineering Science* 2006, 61, 218-228.
- [14] Gelves, R., Dietrich, A., Takors, R., Modeling of gas-liquid mass transfer in a stirred tank bioreactor agitated by a Rushton turbine or a new pitched blade impeller. *Bioprocess and Biosystems Engineering* 2014, 37, 365.
- [15] Wang, H., Jia, X., Wang, X., Zhou, Z., *et al.*, CFD modeling of hydrodynamic characteristics of a gas-liquid two-phase stirred tank. *Applied Mathematical Modelling* 2014, 38, 63-92.
- [16] Xie, R., Li, J., Jin, Y., Zou, D., Chen, M., Simulation of drop breakage in liquid-liquid system by coupling of CFD and PBM: Comparison of breakage kernels and effects of agitator configurations. *Chinese Journal of Chemical Engineering* 2019, 27, 1001-1014.
- [17] Sarhan, A. R., Naser, J., Brooks, G., CFD Modeling of Three-phase Flotation Column Incorporating a Population Balance Model. *Procedia Engineering* 2017, 184, 313-317.
- [18] McClure, D. D., Kavanagh, J. M., Fletcher, D. F., Barton, G. W., Oxygen transfer in bubble columns at industrially relevant superficial velocities: Experimental work and CFD modelling. *Chemical Engineering Journal* 2015, 280, 138-146.
- [19] Laakkonen, M., Moilanen, P., Alopaeus, V., Aittamaa, J., Modelling local bubble size distributions in agitated vessels. *Chemical Engineering Science* 2007, 62, 721-740.

- [20] Bach, C., Yang, J., Larsson, H., Stocks, S. M., *et al.*, Evaluation of mixing and mass transfer in a stirred pilot scale bioreactor utilizing CFD. *Chemical Engineering Science* 2017, 171, 19-26.
- [21] Brucato, A., Ciofalo, M., Grisafi, F., Micale, G., Numerical prediction of flow fields in baffled stirred vessels: A comparison of alternative modelling approaches. *Chemical Engineering Science* 1998, 53, 3653-3684.
- [22] Murthy, B. N., Ghadge, R. S., Joshi, J. B., CFD simulations of gas–liquid–solid stirred reactor: Prediction of critical impeller speed for solid suspension. *Chemical Engineering Science* 2007, 62, 7184-7195.
- [23] Ahmed, S. U., Ranganathan, P., Pandey, A., Sivaraman, S., Computational fluid dynamics modeling of gas dispersion in multi impeller bioreactor. *Journal of Bioscience & Bioengineering* 2010, 109, 588-597.
- [24] Gentric, C., Mignon, D., Bousquet, J., Tanguy, P. A., Comparison of mixing in two industrial gas–liquid reactors using CFD simulations. *Chemical Engineering Science* 2005, 60, 2253-2272.
- [25] Jian, M., Yuyun, B., Lei, C., John, M. S., Zhengming, G., Numerical Simulation of Gas Dispersion in an Aerated Stirred Reactor with Multiple Impellers. *Industrial & Engineering Chemistry Research* 2008, 47, 7112-7117.
- [26] Kerdouss, F., Bannari, A., Proulx, P., Bannari, R., *et al.*, Two-phase mass transfer coefficient prediction in stirred vessel with a CFD model. *Computers and Chemical Engineering* 2008, 32, 1943-1955.
- [27] Sarkar, J., Kanwar, L., Loomba, V., Rathore, A., CFD of mixing of multiphase flow in a bioreactor using population balance model. *Biotechnology Progress* 2016, 32, n/a-n/a.
- [28] Hong, H.-S., Simulation of gas-inducing reactor couples gas–liquid mass transfer and biochemical reaction. *Biochemical engineering journal* 2014, v. 91, pp. 1-9-2014 v.2091.
- [29] Hsu, R.-C., Chiu, C.-K., Lin, S.-C., A CFD study of the drawdown speed of floating solids in a stirred vessel. *Journal of the Taiwan Institute of Chemical Engineers* 2018, 90, 33-43.
- [30] González-Sáiz, J.-M., Garrido-Vidal, D., Pizarro, C., Scale up and design of processes in aerated-stirred fermenters for the industrial production of vinegar. *Journal of Food Engineering* 2009, 93, 89-100.
- [31] BAO Yuyun, H. X., SHI Litian, WANG Yingchen, Mechanism of Off-Bottom Suspension of Solid Particles in a Mechanical Stirred Tank. *Chinese Journal of Chemical Engineering* 2002, 10, 476-479.
- [32] Bao, Y., Hao, Z., Gao, Z., Shi, L., Smith, J. M., Suspension of buoyant particles in a three phase stirred tank. *Chemical Engineering Science* 2005, 60, 2283.
- [33] Julian Becker, P., Puel, F., Jakobsen, H. A., Sheibat-Othman, N., Development of an improved breakage kernel for high dispersed viscosity phase emulsification. *Chemical Engineering Science* 2014, 109, 326-338.
- [34] Cheung, S. C. P., Yeoh, G. H., Tu, J. Y., On the modelling of population balance in isothermal vertical bubbly flows—Average bubble number density approach. *Chemical Engineering & Processing: Process Intensification* 2007, 46, 742-756.
- [35] Montoya, G., Sanyal, J., Braun, M., Azhar, M., On the assessment, implementation, validation, and verification of drag and lift forces in gas–liquid applications for the CFD codes FLUENT and CFX. *Experimental and Computational Multiphase Flow* 2019, 1, 255-270.
- [36] Frank, T., Shi, J., Burns, A. D., *Proceeding of the Third International Symposium on Two-Phase Modelling and Experimentation, Pisa, Italy*, Citeseer 2004, pp. 22-25.
- [37] Xie, M., Xia, J., Zhou, Z., Chu, J., *et al.*, Flow Pattern, Mixing, Gas Holdup and Mass Transfer Coefficient of Triple-Impeller Configurations in Stirred Tank Bioreactors. *Industrial & Engineering Chemistry Research* 2014, 53, 5941-5953.
- [38] Jamshidian, R., Scully, J., Van den Akker, H. E. A., Two-fluid simulations of an aerated lab-scale bioreactor. *Chemical Engineering Research & Design: Transactions of the Institution of Chemical Engineers Part A* 2023, 196, 254-275.

- [39] Lane, G. L., Schwarz, M. P., Evans, G. M., Numerical modelling of gas–liquid flow in stirred tanks. *Chemical Engineering Science* 2005, *60*, 2203-2214.
- [40] Wang, H., Gao, Z., Wang, B., Bao, Y., Cai, Z., Gas dispersion and solid suspension in a three-phase stirred tank with triple impellers. *Chinese Journal of Chemical Engineering* 2020, *28*, 1195-1202.
- [41] Fújasová, M., Linek, V., Moucha, T., Mass transfer correlations for multiple-impeller gas–liquid contactors. Analysis of the effect of axial dispersion in gas and liquid phases on “local” [formula omitted] values measured by the dynamic pressure method in individual stages of the vessel. *Chemical Engineering Science* 2007, *62*, 1650-1669.
- [42] Arjunwadkar, S. J., Saravanan, K., Pandit, A. B., Kulkarni, P. R., Optimizing the impeller combination for maximum holdup with minimum power consumption. *Biochemical Engineering Journal* 1998, *1*, 25-30.
- [43] Bernauer, S., Schöpf, M., Eibl, P., Witz, C., *et al.*, Characterization of the gas dispersion behavior of multiple impeller stages by flow regime analysis and CFD simulations. *Biotechnology and Bioengineering* 2021, *118*, 3058.
- [44] Wang, W., Mao, Z.-S., Yang, C., Experimental and Numerical Investigation on Gas Holdup and Flooding in an Aerated Stirred Tank with Rushton Impeller. *Industrial & Engineering Chemistry Research* 2006, *45*, 1141-1151.
- [45] Ferreira, P., Lopes, M., Mota, M., Belo, I., Oxygen mass transfer impact on citric acid production by *Yarrowia lipolytica* from crude glycerol. *Biochemical Engineering Journal* 2016, *110*, 35-42.
- [46] Palmerín-Carreño, D. M., Castillo-Araiza, C. O., Rutiaga-Quíñones, O. M., Verde-Calvo, J. R., Huerta-Ochoa, S., Kinetic, oxygen mass transfer and hydrodynamic studies in a three-phase stirred tank bioreactor for the bioconversion of (+)-valencene on *Yarrowia lipolytica* 2.2ab. *Biochemical Engineering Journal* 2016, *113*, 37-46.
- [47] Santos, A. G., Ribeiro, B. D., do Nascimento, F. V., Coelho, M. A. Z., Culture Miniaturization of Lipase Production by *Yarrowia lipolytica*. *Current Biochemical Engineering* 2019, *5*, 12-20.
- [48] Lone, S. R., Kumar, V., Seay, J. R., Englert, D. L., Hwang, H. T., Mass Transfer and Rheological Characteristics in a Stirred Tank Bioreactor for Cultivation of *Escherichia coli* BL21. *Biotechnology and Bioprocess Engineering* 2020, *25*, 766.
- [49] Guo, D.-S., Ji, X.-J., Ren, L.-J., Li, G.-L., *et al.*, Development of a scale-up strategy for fermentative production of docosahexaenoic acid by *Schizochytrium* sp. *Chemical Engineering Science* 2018, *176*, 600-608.
- [50] Abujelala, M. T., Lilley, D. G., Limitations and Empirical Extensions of the k - ϵ Model As Applied To Turbulent Confined Swirling Flows. *Chemical Engineering Communications* 1984, *31*, 223-236.
- [51] Olmos, E., Gentric, C., Vial, C., Wild, G., Midoux, N., Numerical simulation of multiphase flow in bubble column reactors. Influence of bubble coalescence and break-up. *Chemical Engineering Science* 2001, *56*, 6359-6365.
- [52] Khopkar, A. R., Kasat, G. R., Pandit, A. B., Ranade, V. V., CFD simulation of mixing in tall gas–liquid stirred vessel: Role of local flow patterns. *Chemical Engineering Science* 2006, *61*, 2921-2929.
- [53] McClure, D. D., Kavanagh, J. M., Fletcher, D. F., Barton, G. W., Development of a CFD Model of Bubble Column Bioreactors: Part Two – Comparison of Experimental Data and CFD Predictions. *Chemical Engineering & Technology* 2014, *37*, 131-140.
- [54] Simonnet, M., Gentric, C., Olmos, E., Midoux, N., CFD simulation of the flow field in a bubble column reactor: Importance of the drag force formulation to describe regime transitions. *Chemical Engineering & Processing* 2008, 1726.
- [55] Liao, Y., Update to the MUSIG model in ANSYS CFX for reliable modelling of bubble coalescence and break-up. *Applied Mathematical Modelling* 2020, *81*, 506-521.

- 1 [56] Vakili, M. H., Esfahany, M. N., CFD analysis of turbulence in a baffled stirred tank, a three-
2 compartment model. *Chemical Engineering Science* 2009, **64**, 351-362.
- 3 [57] Andersson, R., Andersson, B., On the Break-up of Fluid Particles in Turbulent Flows. *AIChE*
4 *Journal* 2006, **52**, 2020-2030.
- 5 [58] Liu, H., Li, M., Two-compartmental population balance modeling of a pulsed spray fluidized
6 bed granulation based on computational fluid dynamics (CFD) analysis. *International Journal of*
7 *Pharmaceutics* 2014, **475**, 256-269.
- 8 [59] Liu, H., Yoon, S., Li, M., Three-dimensional computational fluid dynamics (CFD) study of the
9 gas-particle circulation pattern within a fluidized bed granulator: By full factorial design of
10 fluidization velocity and particle size. *Drying Technology* 2017, **35**, 1043-1058.
- 11 [60] Khalil, A., Rosso, D., DeGroot, C. T., Effects of flow velocity and bubble size distribution on
12 oxygen mass transfer in bubble column reactors—A critical evaluation of the computational fluid
13 dynamics-population balance model. *Water Environment Research (10614303)* 2021, **1**.
- 14 [61] Bhole, M. R., Joshi, J. B., Ramkrishna, D., CFD simulation of bubble columns incorporating
15 population balance modeling. *Chemical Engineering Science* 2008, **63**, 2267-2282.
- 16 [62] Zadghaffari, R., Moghaddas, J. S., Revstedt, J., Large-eddy simulation of turbulent flow in a
17 stirred tank driven by a Rushton turbine. *Computers and Fluids* 2010, **39**, 1183-1190.
- 18 [63] Sun, K., Zhao, H., Zhao, K., Li, D., Bai, S., Optimization of SCR inflow uniformity based on
19 CFD simulation. *Open Physics* 2020, **18**, 1168-1177.

1 TABLES

2 **TABLE 1** Mathematical models used in CFD and PBM equations.

Model Applied	Equations	Remarks
Eulerian- Eulerian multiphase model	$\alpha_i + \alpha_g + \alpha_o = 1 \quad (8)$ $\frac{\partial}{\partial t}(\rho_i \alpha_i) + \nabla(\rho_i \alpha_i \bar{u}_i) = 0 \quad (9)$ $\frac{\partial}{\partial t}(\rho_i \alpha_i \bar{u}_i) + \nabla(\rho_i \alpha_i \bar{u}_i \bar{u}_i) = -\alpha_i \nabla p + \nabla(\alpha_i \mu_i (\nabla \bar{u}_i + (\bar{u}_i)^T)) + \sum \bar{M}_{ii}^{drag} + \bar{F}_i + \alpha_i \rho_i \bar{g} \quad (10)$ $F_i = -2\alpha_i \rho_i \bar{\omega} \times \bar{u}_i - \alpha_i \rho_i \bar{\omega} \times (\bar{\omega} \times \bar{r}) \quad (11)$ $\frac{\partial}{\partial t} n_i + \frac{\partial}{\partial t} \nabla(n_i \bar{u}_i) = P_B - D_B + P_C - D_C \quad (12)$ $n_i(t) = \int_{v_{i-\frac{1}{2}}}^{v_{i+\frac{1}{2}}} n(v, t) dv \quad (13)$ $\frac{\partial}{\partial t}(\rho_o \alpha_o f_i) + \nabla(\rho_o \alpha_o \bar{u}_o f_i) = S_i \quad (14)$	<p>Extensive use in this type of system [15, 23, 51].</p> <p>In isothermal bubbly flows, interfacial momentum transfer dominates the multiphase-momentum equations primarily affected by drag [34]. The non-drag forces have not been enabled [23, 28, 52, 53].</p> <p>In the MFR method, the constant angular velocity (ω) impeller rotation adds additional momentum in the F_{ii} form.</p> <p>The general form of the population balance was solved along with the Eulerian-Eulerian model to describe particle continuity.</p> <p>Discretizing the above equation into size groups and further integrating over the bin size dimension and group's mass, the summation of source terms must equal zero.</p>
k- ϵ Turbulence Models	$\mu_{ti} = c_\mu \rho_i \left(\frac{k_i^2}{\epsilon_i} \right) \quad (15)$ $\frac{\partial(\alpha_i \rho_i k_i)}{\partial t} + \nabla \left(\alpha_i \left(\rho_i k_i \bar{u}_i - \left(\mu_i + \frac{\mu_{ti}}{\sigma_k} \right) \nabla k_i \right) \right) = \alpha_i (P_i - \rho_i \epsilon_i) \quad (16)$ $\frac{\partial(\alpha_i \rho_i \epsilon_i)}{\partial t} + \nabla \left(\alpha_i \rho_i \epsilon_i \bar{u}_i - \left(\mu_i + \frac{\mu_{ti}}{\sigma_\epsilon} \right) \nabla \epsilon_i \right) = \alpha_i \frac{\epsilon_i}{k_i} (C_{\epsilon 1} P_i - C_{\epsilon 2} \rho_i \epsilon_i) \quad (17)$	<p>k- ϵ model was applied for continuous phase turbulent effects. The dispersed phase zero equation was used for dispersed phases [50, 54].</p> <p>Important to note that if the k- ϵ were applied to all three phases, volume-based mixture values for density, viscosity, and velocity would be required to integrate the turbulence equations into the transport equations (Le et al., 2018); however, due to the small oil and gas volume fractions, the continuous liquid's turbulence is the dominating factor.</p>
Drag Force	$C_D = \begin{cases} \frac{24(1 + 0.15 Re^{0.687})}{Re}, & Re \leq 1000 \\ 0.44, & Re > 1000 \end{cases} \quad (18)$ $\bar{M}_{i,dp}^{drag} = -\bar{M}_{dp,i}^{drag} = \frac{3}{4} \frac{C_D}{d_{dp}} \alpha_{dp} \rho_l \bar{u}_{dp} - \bar{u}_i (\bar{u}_{dp} - \bar{u}_i) \quad (19)$ $C_{D(ellipse)} = \frac{4}{3} \frac{g d_b \rho_l - \rho_g}{U_T^2 \rho_l} \quad (20)$ $U_T = \frac{\mu_l}{\rho_l d_g} M^{-0.149} (J - .857) \quad (21)$ $J = \begin{cases} .94 H^{7.57}, & 2 < H \leq 59.3 \\ 3.42 H^{4.41}, & H > 59.3 \end{cases} \quad (22)$ $H = \frac{4}{3} E_o M^{-.149} \left(\frac{\mu_l}{\mu_{ref}} \right)^{-0.14} \quad (23)$	<p>C_D models the complex dependencies of shape, inclination and flow conditions on hydrodynamic bubbles/droplets (Montoya et al., 2019).</p> <p>Oil C_D is calculated with the Schiller Naumann Drag correlation (Eq. 14) (Ishii & Zuber, 1979).</p> <p>The Grace correlation was applied to an air bubble and was developed for air-water systems. It accounts for the geometric change of constant effective diameter bubbles (Clift et al., 2005).</p>
PBM	$C_D = \max(C_D(sphere), \min(C_D(ellipse), C_D(cap))) \quad (24)$ $B_K = .923 F_B (1 - \alpha_o) \left(\frac{\epsilon_c}{d_i^2} \right)^{\frac{1}{3}} \int_{\epsilon_{min}}^1 \frac{(1 + \xi)^2}{\xi^{11/3}} e^{-\left(\frac{12(f_{BV}^{\frac{2}{3} + (1-f_{BV})^{\frac{2}{3}-1}})}{2\rho_c \epsilon_c^{2/3} d_i^{5/3} \xi^{11/3}} \right) \sigma} d\xi \quad (25)$ $Q(V_i; V_j) = \left(F_{CT} \frac{\pi}{4} (d_i + d_j)^2 (2\epsilon_i^{\frac{2}{3}} d_i^{\frac{2}{3}} + u_{ij}^2)^{\frac{1}{2}} + F_{CB} \frac{\pi}{4} (d_i + d_j)^2 \left U_{rj} - \sqrt{\frac{2.14\sigma}{\rho_l d_i} + .505 g d_i} \right \right) e^{-\frac{t_{ij}}{\tau_{ij}}} \quad (26)$	<p>For sparsely distributed particles, CFX automatically counts the spherical particle and spherical cap limited by Eq 20.</p> <p>Well-demonstrated application [12, 55-59]</p>
Power	$t_{ij} = \left(\frac{\rho_l r_{ij}^3}{16\sigma} \right)^{\frac{1}{2}} \ln \left(\frac{h_0}{h_f} \right) \quad (27)$ $\tau_{ij} = \frac{r_{ij}^3}{\epsilon_c^{\frac{1}{3}}} \quad (28)$ $r_{ij} = 2 \left(\frac{1}{r_i} + \frac{1}{r_j} \right)^{-1} \quad (29)$ $\Gamma = \sum_i (\Delta \rho)_i A_i r_i \quad (30)$	<p>Collision efficiency is modeled with a comparison of t_{ij} and actual contact time during the collision (τ_{ij}). This model has been shown to produce accurate results for coalescence in Euler-Euler two-fluid model with an integrated population balance model [60] but may sometimes over-predict coalescence [61], which may impact mass transfer calculations.</p>
Uniformity	$P = 2\pi\omega\Gamma \quad (31)$ $\phi = 1 - \frac{\int_0^{Rx Vol} \alpha_i - \alpha_{i avg} }{2 * \int_0^{Rx Vol} \alpha_i} \quad (32)$	<p>Power numbers were derived by utilizing Ansys' built-in torque (Γ) capabilities to calculate utilizing the formula in Eq. 26. [62]</p> <p>Uniformity indexes (ϕ) help quantitatively demonstrate the reactors' dispersed phase distributions [63]</p>

3

4

FIGURE LEGENDS

FIGURE 1 Pictorial of the basic simulation BCs, setup, and flow for this CFD study (A). Illustration of the 1-L working volume glass bioreactor with key dimensions noted for the PBI (B) and Rushton impeller (C) setups.

FIGURE 2 Oil volume fraction contours for MFR 3R (A–D) and PBI (E–H) and SM approach 3R (I–L) and PBI (M–P) impeller setups in the 1-L working volume bioreactor.

FIGURE 3 Experimental validation bioreactor runs with the CFD average air particle sizes imposed into the pictures for 3R (top row) and PBI (bottom row) impeller setups. The 1000-RPM stirring speed runs were excluded due to their similarity (pictorially and particle size similarity) to the 1200-RPM stirring speed runs (A). An experimental oil mixing comparison was captured with a Canon EOS 6D Mark II between oil flow pattern development with PBI (left) and 3R (right) impeller setups (B). The liquid volume was set at 1 L for all simulations.

FIGURE 4 Comparison of air/water CFD simulations to the Xie et al. correlation gas holdup [37] as a function of power input (P/V) (A). Experimental and air/ water CFD simulation gas holdup comparison as a function of power input (P/V) (B). Three-phase (headspace included) experimental and CFD gas holdup as a function of power input (P/V) [37] (C). The CFD calculated $C_k k_L a_{PT}$ as a function of P/V for three-phase (air, oil, and water) simulations. The liquid volume was set at 1 L for all simulations.

FIGURE 5 Oil volume fraction contours for the 3R (A & B) and PBI (C & D) impeller setups for the three-phase (air, oil, and water), 1000- and 1200-RPM simulations (most relevant for high-cell density fermentation with *Yarrowia lipolytica*). Air volume fraction contours for the 3R (E & F) and (G&H). Note: headspaces are not included for easier comparison to two-phase simulations. The liquid volume was set at 1 L for all simulations.

NOMENCLATURE

Greek Symbols

α	Volume Fraction
Γ	Torque
ξ	Dimensionless size of eddies in the inertial subrange of turbulence
ε	Turbulence dissipation rate
ϕ	Uniformity index
ρ	Density of phase
μ	Viscosity
μ_{eff}	Effective viscosity accounting for turbulence
σ	Surface Tension Coefficient (Air/Water = .072 and Oil/Water = .050 $\frac{N}{m}$)
σ_k	Turbulent Prandtl Number (kinetic energy) = 1.00

σ_ε	Turbulent Prandtl Number (kinetic energy dissipation) = 1.30
u_i	Mean Velocity
$\overline{\tau}_l$	Reynolds stress tensor
τ_{ij}	Actual collision contact time
ω	Rotational Speed (rev/s)

1

Nomenclature

a_g	Interfacial surface area from the predicted bubble size
A_i	Area of the surface
B_K	Break-up Kernel
BC	Boundary Condition
C	Constants
C_D	Drag coefficient
C_k	Volumetric mass transfer coefficient constant
$C_{\varepsilon 1}$	Reynolds Stress model constant = 1.45
$C_{\varepsilon 2}$	Reynolds Stress model constant = 1.9
C_o	Actual dissolved oxygen concentration
C_o^*	Saturated dissolved oxygen concentration
c_μ	k - ε turbulence model constant = .09
D	Diffusion coefficient of oxygen in water ($1.98\text{e-}9 \frac{\text{m}^2}{\text{s}}$)
D_B	Death rate of a dispersed phase due to break-up
D_C	Death rate of a dispersed phase to coalescence
D_I	Impeller diameter (m)
D_T	Tank diameter
d	Bubble diameter
d_{bg}	Local Sauter mean bubble diameter
d_i	Diameter of bubble/droplet in bin I or (j)
E_o	Eötvös number
f_i	Size group fraction of the i th bubble group

f_{BV}	Break-up fraction (dimensionless)
F	Calibration coefficient
\vec{F}_l	Coriolis and centrifugal forces
\vec{g}	Gravitational acceleration constant
h_f	Critical rupture thickness
h_0	Initial film thickness
H	Empirical M and E_o functions
J	Empirical M and E_o functions
k	Turbulence kinetic energy
k_L	Liquid mass transfer resistance
$k_L a$	Volumetric mass transfer coefficient
K_i	Exchange coefficient of liquid and polydispersed phases (oil and water)
l	Liquid phase (water)
m	Mass
\dot{m}	Mass flowrate
M	Morton number
M_i	Interphase momentum exchange term
MUSIG	Multiple size group
N_P	Power number
o	Oil phase (corn oil)
n_i	Density of particles of mass m at time t .
$(\Delta_P)_i$	Pressure difference around the impeller at surface I
p	Pressure
P	Power
P_B	Production rate of a dispersed phase due to break-up
P_C	Production rate of a dispersed phase to coalescence
P_l	Turbulent kinetic energy due to shear
PBM	Population balance modeling
OUR	Oxygen uptake rate
OTR	Oxygen transfer rate

r_i	Radial distance from the axis of the mounted impeller shaft
r_{ij}	Equivalent radius
Re	Reynolds number
\vec{R}_i	Interfacial momentum
RMS	Root mean square
S_i	Source terms
SM	Sliding mesh approach
t	Time
t_{ij}	Time required for coalescence between particle i and j
TSF	Time scale factor
u	Velocity
U_T	Terminal bubble velocity
v	Mass volume fraction of size group i
V	Reactor volume
vvm	Volume of gas per volume of unaerated liquid per minute
W_I	Impeller width (Vertical Distance)
W_B	Width of the baffle (From OD to ID)

1

Subscripts

c	Continuous phase
dp	Dispersed phase (oil or gas)
e	Experimentally estimated
i	Mother (particle to be broken into smaller (daughter particles)
j	Daughter (particle originating from break-up of larger (mother) particle
l	Liquid phase (continuous phase, water)
g	Gas phase (dispersed phase, air bubbles)
o	Oil phase (polydispersed phase, oil droplets)
PT	Higbie's penetration theory
P	Power
r	Location vector

R	Lubrication
t	Turbulent

Superscripts

$drag$	Drag
B	Buoyancy
P	Dispersion forces

1

2